Atomic defects and doping of monolayer NbSe2

Nguyen, L.; Komsa, H.-P.; Khestanova, E.; Kashtiban, R.; Peters, J. P.; Lawlor1, S.; Sanchez, A. M.; Sloan, J.; Gorbachev, R.; Grigorieva, I.; Krasheninnikov, A. V.; Haigh, S. J.;

Originally published:

February 2017

ACS Nano 11(2017), 2894-2904

DOI: https://doi.org/10.1021/acsnano.6b08036

Atomic Defects and Doping of Monolayer $NbSe_2$

Journal:	*ACS Nano*
Manuscript ID	nn-2016-080367.R3
Manuscript Type:	Article
Date Submitted by the Author:	13-Feb-2017

Complete List of Authors:	Nguyen, Lan; University of Manchester, School of Materials Komsa, Hannu-Pekka; Aalto University, Department of Applied Physics Khestanova, Ekaterina; University of Manchester, School of Physics & Astronomy Kashtiban, Reza; The University of Warwick, Department of Physics Peters, Jonathan; The University of Warwick, Department of Physics Lawlor, Sean; University of Manchester, School of Materials Sanchez, Ana M.; University of Warwick, Department of Physics Sloan, Jeremy; University of Warwick, Department of Physics Gorbachev, Roman; University of Manchester, School of Physics & Astronomy Grigorieva, Irina; University of Manchester, The School of Physics and Astronomy Krasheninnikov, Arkady; Helmholtz-Zentrum Dresden-Rossendorf, Ion Beam Centre ; National University of Science and Technology MISiS; Aalto University, Department of Applied Physics Haigh, Sarah; University of Manchester, School of Materials

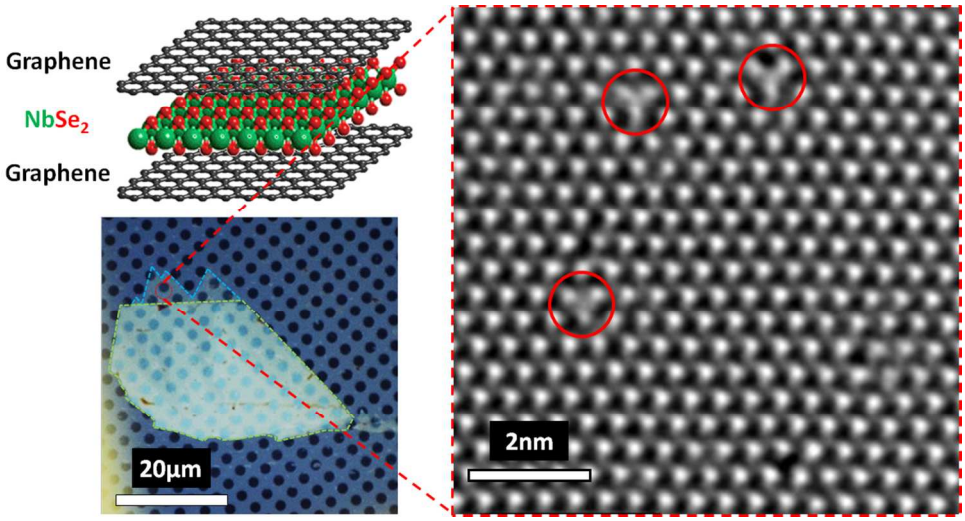

103x52mm (300 x 300 DPI)

Atomic Defects and Doping of Monolayer $NbSe_2$

*Lan Nguyen[1], Hannu-Pekka Komsa[2], Ekaterina Khestanova[3], Reza J. Kashtiban[4], Jonathan J.P. Peters[4], Sean Lawlor[1], Ana M. Sanchez[4], Jeremy Sloan[4], Roman V. Gorbachev[3], Irina V. Grigorieva[3], Arkady V. Krasheninnikov[5,6,7], Sarah J. Haigh[1]**

Corresponding Author

*sarah.haigh@manchester.ac.uk

1. School of Materials, University of Manchester, Oxford Road, M13 9PL, United Kingdom

2. COMP Centre of Excellence, Department of Applied Physics, Aalto University, P.O. Box 11100, FI-00076 Aalto, Finland

3. School of Physics and Astronomy, University of Manchester, Oxford Road, M13 9PL, United Kingdom

4. Department of Physics, University of Warwick, Coventry, CV4 7AL, United Kingdom

5. Helmholtz-Zentrum Dresden-Rossendorf, Institute of Ion Beam Physics and Materials Research, 01328 Dresden, Germany

6. National University of Science and Technology MISiS, Leninskiy Prospekt, Moscow, 119049, Russian Federation

7. Department of Applied Physics, Aalto University, P.O. Box 11100, FI-00076 Aalto, Finland

KEYWORDS: Air-sensitive 2D Crystals, Graphene Encapsulation, Monolayer $NbSe_2$, Transition Metal Dichalcogenides, Atomic Resolution TEM, Defect Dynamics, Pt Doping

ABSTRACT: We have investigated the structure of atomic defects within monolayer $NbSe_2$ encapsulated in graphene by combining atomic-resolution transmission electron microscope (TEM) imaging, density functional theory (DFT) calculations and strain mapping using geometric phase analysis (GPA). We demonstrate the presence of stable Nb and Se monovacancies in monolayer material and reveal that Se monovacancies are the most frequently observed defect, consistent with DFT calculations of their formation energy. We reveal that adventitious impurities of C, N and O can substitute into the $NbSe_2$ lattice stabilizing Se divacancies. We further observe evidence of Pt substitution into both Se and Nb vacancy sites. This knowledge of the character and relative frequency of different atomic defects provides the potential to better understand and control the unusual electronic and magnetic properties of this exciting two-dimensional material.

Two-dimensional (2D) crystals such as graphene and the transition metal dichalcogenides (TMDCs) have attracted considerable scientific interest in recent years due to their unique properties and potential for revolutionary technological applications.[1-3] Aberration-corrected transmission electron microscopy (TEM) techniques have played a crucial role in unravelling the structure-property relationships of these materials at the atomic level.[4-9] In particular, TEM can reveal the presence of local deviations from the pristine atomic structure, such as intrinsic defects, dislocations or dopant atoms, which can directly affect the properties of the material.[4-9]

Recent work has reported the tailoring of the electronic and functional properties of 2D crystals by deliberately introducing defects and/or doping the material with foreign atoms.[5, 8, 10-17] This offers promising pathways for engineering 2D crystals to a broad range of applications in sensors and electronics.[18-20] In particular, the nanoscale engineering of magnetic properties of 2D crystals *via* substitutional doping is a promising research area. [5, 10, 12, 13, 16, 17]

Niobium diselenide ($NbSe_2$) is a 2D crystal which is gathering much attention; it demonstrates superconductivity at low temperatures (<10K)[21-25], charge density wave formation from ≤33K in bulk to ≤145K in the monolayer[22, 26-29] and excellent photoconductivity.[30] Like the more commonly studied TMDCs, $NbSe_2$ has a trigonal prismatic crystal structure with strong covalent bonding of Se-Nb-Se atoms within the plane and weak van-der Waals bonding between layers, allowing for mechanical[21, 24, 25, 31, 32] and liquid exfoliation[33] of ultrathin sheets. However, understanding and optimising the unique properties of $NbSe_2$ has been held back by the severe degradation of the material, which occurs under ambient conditions when exfoliated to a few layers.[21, 31, 34, 35]

We have recently demonstrated superconductivity for an exfoliated monolayer material by studying $NbSe_2$ monolayers.[31] This was achieved by preparing samples using mechanical exfoliation in a highly controlled inert glove box environment, coupled with encapsulation using structurally stable 2D materials (graphene or hexagonal BN) and tunnelling contacts. The encapsulation protects the $NbSe_2$ from the environment preserving superconducting properties, whereas no transition to the superconducting phase was observed for monolayers prepared under ambient conditions. Curiously, a number of properties change dramatically from bilayer $NbSe_2$ to monolayer, such as a significant drop in the superconducting transition temperature[31] and the increase of temperature at which charge density waves (CDW)[26] are observed. The origin of this behaviour remains unknown, but a likely hypothesis is that it is related to atomic scale defects, the nature of which could be elucidated by structural studies. Only by understanding the degradation of such materials at the atomic level can their properties be fully realised and exploited.

A recent scanning tunnelling microscopy study has shown that defects in bulk $NbSe_2$ play a crucial role in stabilising nanoscale regions of CDW order at temperatures higher than the bulk CDW transition temperature.[36] These nanoscale regions of CDW ordering increase in size as the temperature is lowered, until the CDW phase persists throughout the crystal.[36] Despite the importance of these defects, to our knowledge no-one has yet studied defects in monolayer $NbSe_2$ material. TEM provides a complementary approach for atomic scale imaging, and can be combined with spectroscopic imaging techniques to gain information on local elemental distribution and electronic structure.[37, 38] However to date, the difficulty of preparing representative samples has limited electron microscopy studies of $NbSe_2$ to relatively low resolution imaging and electron diffraction.[39, 40] Here, using graphene encapsulation to preserve the structure we provide atomic resolution TEM imaging of monolayer $NbSe_2$. The presence of the graphene sheets preserves the lattice structure of the

material for more than 10 months in ambient conditions; in stark contrast to unprotected samples which degrade after a few hours. However, when imaged at the atomic scale we find the encapsulated $NbSe_2$ contains significant populations of atomic defects which are not the simply the result of electron beam irradiation. We correlate our experimental imaging results with extensive density functional theory (DFT) investigations of defect formation energies.

Results/Discussion

To prepare specimens for TEM investigations, thin $NbSe_2$ flakes were exfoliated in an inert environment and encapsulated between two graphene sheets (Figure 1b) before being transferred onto gold quantifoil grids.[41] The thinnest regions of such flakes were investigated by selected-area electron diffraction (SAED) in the TEM (Figure 1d). Our multislice calculations[42] show that by analysing the ratio of the first $\{\bar{1}010\}$ and second order $\{\bar{2}110\}$ diffraction spot intensities it is possible to identify monolayer regions of $NbSe_2$ similar to previous electron diffraction experiments performed on 2D crystals.[43-47] These simulations show that the ratio of $\{\bar{1}010\}/\{\bar{2}110\}$ diffraction spot intensities has a value of 1.16 for monolayer $NbSe_2$, 0.01 for bilayer, and 0.16 for trilayer. For thicker samples the values of these ratios continue to decrease in an oscillatory fashion attenuating close to zero for even numbers of layers as shown in supporting information Figure S1 (in addition to similar values obtained from the $\{0\ \bar{1}\ 10\}/\{\ \bar{2}110\ \}$). Our experimental results show a $\{\bar{1}010\}/\{\bar{2}110\}$ intensity ratio of 0.56. This is much higher than would be obtained for bilayer or thicker flakes indicating that the region captured by the 40 μm diameter SAED aperture must contain largely monolayer material. That this is less than the 1.16 predicted for perfect monolayer suggests that the ~1um diameter region sampled also contained some few-layer $NbSe_2$. We have further confirmed the thinnest sample regions to be monolayer using atomic resolution focal series TEM imaging and simulations (SI Figure S2).

Aberration corrected low voltage TEM imaging (80kV) revealed the atomic structure of our encapsulated monolayer $NbSe_2$. Figure 2 shows examples of the different types of vacancy defects that were observed experimentally, together with comparison to image simulations produced from our DFT optimised atomic models for vacancies in this material. Such analysis allows us to determine the nature of different types of atomic vacancies, demonstrating a good agreement between experimental images and simulations for niobium vacancies (V_{Nb}), selenium monovacancies (V_{Se}) and selenium divacancies, (V_{Se2}), where the two missing selenium atoms are in the same location when viewed normal to the flake along <0001>. Experimental images were low pass filtered to remove the small contrast contributions from the graphene lattice and clearly visualise defects in the $NbSe_2$ lattice (SI Figure S3). Qualitatively, the selenium vacancy defects form white triangles of contrast at Scherzer defocus with a greater increase in intensity for the central selenium site found for selenium divacancies compared to selenium monovacancies. The niobium vacancies appear as triangles of contrast with the opposite orientation to the selenium vacancy features (an increase of intensity on the Nb site compared to the pristine lattice).

Our previous work has demonstrated that even though TMDCs with defects produced by the electron beam are not in thermodynamic equilibrium, the relative abundance of defects and atom displacement energies correlate with defect formation energies.[8, 48] Here we have used DFT to analyse the formation energies for the different vacancies we observe experimentally in $NbSe_2$ (SI Table T1) (for details of modelling see 'Methods' section). At neutral conditions (mid-point between the Se-rich or Nb-rich limits), formation energies for V_{Se} and V_{Nb} monovacancies were found to be 1.05 eV and 3.49 eV respectively. These values are lower than those found for more common TMDCs, *e.g.*, in MoS_2 under similar conditions,[49] which is in agreement with the consensus in the literature that $NbSe_2$ degrades more easily

than these other TMDCs. As well as monovacancies we also observe a significant number of Se divacancies (the relative frequency of different defects is considered later). However, our DFT calculations predict that V_{Se2} has a high formation energy of 3.53 eV. The presence of V_{Se2} defects in the $NbSe_2$ sheet is therefore a puzzle; to reduce the total energy one would expect the crystal to relax to form two V_{Se} defects with the lower combined formation energy ($2V_{Se}$ = 2.09 eV). Furthermore, our first principles calculations show that all vacancy interactions in $NbSe_2$ are repulsive, which would drive apart pairs of Se monovacancies once the divacancy had dissociated (see supplementary material Figure S4).

To explain the presence of significant V_{Se2} defects in our material, we have performed DFT calculations investigating the stability of different elemental substitutions into the V_{Se2} sites. Cu, Si, O, C, N, and H were investigated as these are common contaminants introduced during the exfoliation and flake transfer process. Pt was also included, having been deliberately evaporated on the surface during sample preparation. The heavier elements could quickly be ruled out as TEM image simulations show that these produce a large reduction in contrast (SI Figure S5). We then considered the dissociation energy associated with transforming an impurity-substituted divacancy to an impurity-substituted vacancy and a bare vacancy, *i.e.*, $E_{dis} = [E(X_{Se})+E(V_{Se})]-[E(X_{Se2})+E(pristine)]$, where X is the impurity atom (Table 1). We also consider the case bare divacancy, V_{Se2}, transforming into two bare monovacancies, $2V_{Se}$ (top row Table 1) which is not energetically favourable as discussed above. Similarly, hydrogen substitution has a positive dissociation energy so is unable to stabilize the divacancy. In contrast, C, N, and O impurities all have negative dissociation energies, and thus should lead to stable impurity-substituted divacancies. The availability of C, N and O atoms is assured in such a system from trapped hydrocarbon contamination[41, 50]. C atoms could also be displaced from the encapsulating graphene sheets during electron beam irradiation[51, 52]. Supporting information Figure S6 shows structural DFT models

illustrating how substitutional carbon atoms relax inwards towards the plane of Nb atoms when substituting a Se divacancy. Unfortunately, it is not possible to experimentally verify the presence of light substitutional impurities using our TEM image simulations and linescans as illustrated in Figure 3g-h.

To determine whether the Se divacancies were indeed stabilised by adventitious impurities, we employed geometric phase analysis (GPA)[53] to analyse the strain components surrounding these defects (see methods and SI Figure S7 for details). Figure 3 compares vertical and horizontal strain components from an experimental image of a typical divacancy type defect with the strain predicted from analysis of HRTEM image simulations calculated using our DFT relaxed defect structures. The e_{yx} and e_{yy} strain components show the key characteristics of tension and compression produced in the lattice; only V_{Se2}, H_{Se2}, C_{Se2}, N_{Se2}, O_{Se2}, and V_{Nb} defects are predicted to cause significant strain. Of these, C_{Se2}, N_{Se2} and O_{Se2} match well to the experimental results (Figure 3e, SI Figure S8). This provides experimental evidence supporting our earlier theoretical conclusion that such divacancy defects must be stabilised by C, N or O impurities, and we have chosen to highlight the C-substituted case in Figure 3 since this is the most commonly available of the three impurities. Our DFT calculations predict that oxygen substitution can also stabilise Se monovacancies but these do not produce significant strain on the lattice or contrast for TEM imaging so experimentally it is difficult to distinguish these from bare vacancies.

All TEM studies must consider the potential for electron beam induced defect creation. In this work, all monolayer $NbSe_2$ areas studied were found to be highly defective even after minimal electron dose (received while identifying the correct region of interest using low magnification imaging). In order to study the potential for beam induced defect creation as

well as investigate the relative frequency of occurrence of different types of defects, we have measured changes in the number of defects in response to prolonged electron imaging (Figure 4). The ~175nm^2 region of material analysed here contained 28 V_{Se} monovacancies at initial observation (Figure 4a). V_{Se} was overwhelmingly the most commonly observed point defect; in agreement with our DFT calculations which predict a lower formation energy for V_{Se} compared to the other defects we observed (SI Table T1). After atomic resolution imaging with a typical high electron dose rate ($1.4x10^6 e.Å^{-2}s^{-1}$) for 46s the number of Se monovacancies increases to 42 (Figure 4b). Subsequent imaging with a reduced dose rate ($1x10^3 e.Å^{-2}s^{-1}$) for 43s reduces the number of these defects to 29. This defect population then remains stable even after extended 'high dose rate' ($6.49x10^7 e.Å^{-2}$) exposure (Figure 4d). Under the same imaging conditions, the number of isolated V_{Se2} defects decreases from 11 to 6 and the V_{Nb} defects remains stable at 2). We also observe extended defect regions, the area of which increases slightly throughout imaging from 26.7nm^2 to 32nm^2 (Figure 4a-d). Figures 4e and 4f summarise the observed changes in the numbers and concentrations of each type of defect. The point defect concentration increases initially from 0.82 to 0.98% during high dose rate imaging (from Figure 4a-b), then decreases to 0.70% after low dose rate imaging (Figure 4c) and subsequently is relatively stable. The large number of defects present at first observation, together with the overall reduction in point defects during imaging demonstrates that they are not the result of electron beam damage. We must therefore conclude either that a high proportion of the defects we observe are intrinsic to the crystal, or that defects occur despite the inert conditions used for mechanical exfoliation or that graphene encapsulation only partially stabilises the material.

We now consider the possible mechanism behind our observed increase in the number of V_{Se} point defects during initial high dose rate imaging. TMDCs are often found to be highly

susceptible to knock-on damage but our DFT calculations have demonstrated that at 80kV the energy of the electron beam is well below the knock-on displacement threshold for both Nb and Se in $NbSe_2$ (SI Figure S9), as both species have relatively high atomic masses. Furthermore, we note that beam induced defect formation is likely to be supressed by the encapsulating graphene sheets, which can reduce charging and heating effects as observed during (S)TEM imaging of MoS_2 monolayers.[51, 52] It is feasible that other mechanisms such as chemical etching[54] or a combination of electronic excitations and knock-on damage may facilitate the creation of beam induced defects even at accelerating voltages well below the knock-on damage threshold.[54, 55] Frame-by-frame analysis of TEM image series has demonstrated that many defects are mobile during imaging (Figure 5 and SI Videos V1a-b). This opens up the possibility that defects may migrate into the field of view.. Under low dose rate conditions we observe not a slower increase (as might be expected) but an overall reduction in the number of point defects. We explain this as being a result of the presence of two competing effects: point defect generation and point defect annihilation (or coalescence into larger defective regions). At a low dose rate, the rate of annihilation and/or coalescence of defects must be higher than the rate of defect generation. Vacancy coalescence to form larger extended defects would result in an increase in the total defective area during imaging and this is indeed observed (Figure 4f).

To consider further the potential for coalescence of mobile point defects we have performed a quantitative analysis of point defect clustering for Figure 4a-d in Figure 4g (see SI for details of calculation). The distance between point defects and their next nearest neighbour defect are considered with ‘clusters’ being those occupying nearest neighbour Se columns or second nearest neighbour Se columns. We observe that on average over these images no clustering occurs for ~40% of defects, ~45% of defects are spaced at second nearest neighbour sites and

the remainder ~15% are at next nearest sites. As imaging progressed there was an increasing tendency for defects to be isolated which is in agreement with our DFT predictions for repulsive interactions between defects (SI Figure S4). The most energetically favourable configuration is for second nearest neighbour sites, in agreement with our experimental results. This contrasts with the defect coalescence behaviour observed for other transition metal dichalcogenides such as MoS_2 which preferably form agglomerated lines of adjacent defects.[5] Indeed, we observe that in $NbSe_2$ a line defect can be spontaneously generated but that it is not stable and quickly transforms to a larger defect cluster (Figure 4d).

Closer analysis of the behaviour of the dynamics of individual defect clusters is presented in Figure 5. Figure 5a shows the creation and subsequent annihilation of an isolated Nb vacancy in a pristine region of the crystal. Such defects are rare (Figure 4e) and unstable, which is consistent with their high formation energy predicted from DFT calculations (SI Table T1). Figure 5b illustrates the appearance of a selenium monovacancy within the pristine lattice, which then transforms to a divacancy. This may occur by the formation of an isolated V_{Se} defect, which is then stabilised by a mobile contaminant atom such as C, N or O and then further loss of the other Se atom in the site. However, we have already demonstrated that divacancy defects are unstable and the same process can occur in reverse; as shown in Figure 5c for a defect in a different region of the crystal. These observations further support a mechanism for the formation of Se divacancies as well as their healing which involves a transition to an intermediate energy monovacancy configuration, representing much smaller energy step than the transition straight from pristine to divacancy and vice versa. Figure 5d shows the apparent dynamic movement of a selenium divacancy between adjacent sites together with the appearance of a selenium monovacancy next to the divacancy. This further illustrates the mobility and local interactions of these defects under the electron beam.

We calculated migration barrier for Se vacancy diffusion using nudged elastic band (NEB) method with the results shown in Figure 6a. The calculated migration barriers for V_{Se} diffusion is 0.89 eV and for V_{Se2} dissociating to two neighbouring single vacancies 0.53 eV. Assuming an attempt frequency of 10^{12} 1/s, these correspond to migration rates of 0.001 and 1300 s^{-1} at room temperature. Hence bare double vacancies should readily dissociate. During the aging of several months, significant diffusion is expected. During the imaging, some of the diffusion events may have been activated by the electron beam. The atomic structures show that migrating Se atoms do not show a significant out of plane behaviour suggesting that the encapsulating graphene sheets should not hinder their diffusion.

As vacancies are abundant in our samples, it is worth considering the electronic structure of a single Se vacancy. The calculated band structure and density of states of the system with a Se vacancy are shown in Figure 6b. The states from about -3 eV to -2 eV originate from the Nb-d states. Similar to pristine $NbSe_2$, the Fermi-level fills half of these states, which is responsible for the CDW distortion at low temperatures (cf. SI Figure S10). Vacancies have a small effect on the positions of these states, but results in several localized states in the band gap above the Nb-d manifold, which could make them resolvable with STM. The partial charge densities show that the states originate from a combination of the d-states at the neighbouring Nb atoms.

In an attempt to determine the effectiveness of the graphene encapsulation for protecting the $NbSe_2$, we used energy dispersive X-ray (EDX) spectrum imaging to analyse elemental segregation in the sample after 4 months of ambient storage. Figure 7b-d shows a region of a

graphene encapsulated $NbSe_2$ flake (without Pt) which contains extended strips associated with a high oxygen content. High resolution imaging and diffraction of such regions reveals that in these regions the $NbSe_2$ has transformed to amorphous Nb_2O_5 (See SI Figure S11). Such degradation products have been previously identified by Raman spectroscopy techniques, [21] but not observed at this spatial resolution. Analysis of the orientation of the oxidation strips showed no relationship to the crystal structure of the original $NbSe_2$ but instead the direction corresponded to the one of the encapsulating graphene planes (SI Figure S12). Graphene provides an impermeable barrier to gases [56-58] but only when it makes a perfect seal to the surface. The morphology of the oxidation suggests that there was a crease in the sheet so that the graphene did not form a perfect atomically sharp interface and was therefore unable to protect the $NbSe_2$ from degradation in this region We also reveal an enhancement of oxidation at the step edges of encapsulated flakes (Figure 7). This agrees with DFT calculations for other 2D flakes which have shown that edges are often susceptible to oxidation.[35, 59]

Finally, we consider the substitution of Pt into the $NbSe_2$ lattice as a route to tuning the electronic and magnetic properties of the material. A 0.5nm layer of Pt was originally evaporated on the surface of the encapsulated $NbSe_2$ with the dual aim of producing substitutional defects as well as catalytically reducing surface contamination.[60-62] Figure 8a-b) compares an image simulation of Pt substitution into a Se site shown alongside an atomic resolution TEM image of a typical ‘dark spot’ defect feature found frequently while imaging. However, the distinction between this defect and a Nb atom on a Se site, or other heavy element substitution is difficult to make from high resolution image contrast alone (see SI Figure S5). To solve this problem, we have employed high angle annular dark field (HAADF) STEM imaging, where the contrast is highly sensitive to atomic number. This has

clear advantages when studying heavy atoms on a lighter substrate[55, 63] and already proved highly complementary to TEM imaging many other 2D materials.[7, 64] Figure 8c-d) shows a HAADF simulation and experimental image of a monolayer region, where the direct relationship between intensity and atomic number allows unambiguous identification of the location of Se columns and Nb sites as well as identification of individual Pt atoms in the image. The location of the individual Pt atoms was found to be collocated on either Se or Nb sites within the $NbSe_2$ lattice. Our DFT calculations suggest that Pt substitutions are more energetically favourable than Pt adatoms (SI Table T1), which together with our HAADF-STEM results suggests that Pt has substituted into both Nb and Se sites in the lattice.

The presence of Pt substituted in the $NbSe_2$ lattice might at first seem surprising, as the samples were produced by evaporated Pt on the surface of the encapsulating graphene. However, previous studies have shown metal-mediated etching of graphene can occur under the action of the electron beam.[55, 63, 65-67] This etching of the graphene sheet was visible during TEM imaging (SI Videos V2a-e) and would allow Pt atoms to interact and substitute into the underlying $NbSe_2$ lattice. Furthermore, our calculations indicate that substitutional impurities in either Nb or Se sites can lead to pronounced stabilization of magnetic moment patterns also known as spin density waves (shown in Figure S13). However, since the calculations correspond to 0 K, we cannot assess the stability of these patterns at finite temperatures.

Conclusions

In conclusion, we have observed a wealth of atomic scale defects in graphene encapsulated monolayer $NbSe_2$. We find a high concentration of Se vacancies and divacancies, with the latter being found to be passivated and stabilised with substitutional impurity atoms (C, O or

N). The monolayer material is found to have a high defect density even after a minimal electron dose, and we further observed that the vacancy defect concentration was relatively stable over prolonged electron beam imaging at 80 kV. This suggests that a high proportion of the defects we observe are intrinsic to the crystal or that defects occur despite the inert conditions used for mechanical exfoliation. Graphene encapsulation is found to be essential to preserve the crystal structure of monolayer / few-layer material over prolonged exposure to ambient conditions although creases in the sheets should be avoided to prevent ingress of oxidising species. Substitution of Pt into both Nb and Se sites is found to occur readily opening up a potential pathway for tailoring the intriguing electronic and magnetic properties of $NbSe_2$.

Figures

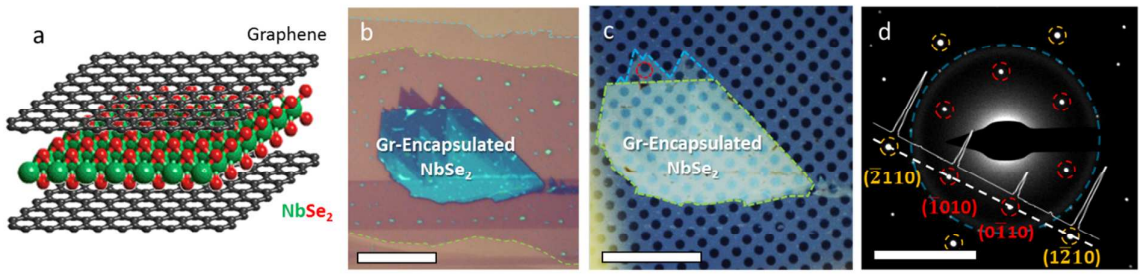

Figure 1: Preparation of graphene encapsulated $NbSe_2$ for TEM imaging by mechanical exfoliation in argon-environment glovebox. (a) Schematic of graphene encapsulated $NbSe_2$ stack. (b) Optical image showing $NbSe_2$ flake encapsulated between graphene sheets on oxidised silicon wafer (scale bar 20 μm). Thin regions were identified by the purple optical contrast. Edges of top and bottom encapsulating graphene sheets are highlighted by green and blue dashed lines. (c) Same Gr-$NbSe_2$-Gr stack transferred to a quantifoil TEM grid. Blue dashed line highlights thinnest $NbSe_2$ region (scale bar: 20μm). (d) SAED pattern from area of red circle in (c), the large blue dashed ring highlights position of graphene $(\bar{1}010)$ reflections (d=0.213nm); small red circles highlight $NbSe_2$ $(\bar{1}010)$ reflections (d=0.296nm); while small orange circles highlight $NbSe_2$, $(\bar{2}110)$, reflections (d=0.173nm). Line profile highlights relative intensities of $(\bar{1}010)$ and $(\bar{2}110)$ diffraction spots used to determine specimen thickness (scale bar: $5nm^{-1}$).

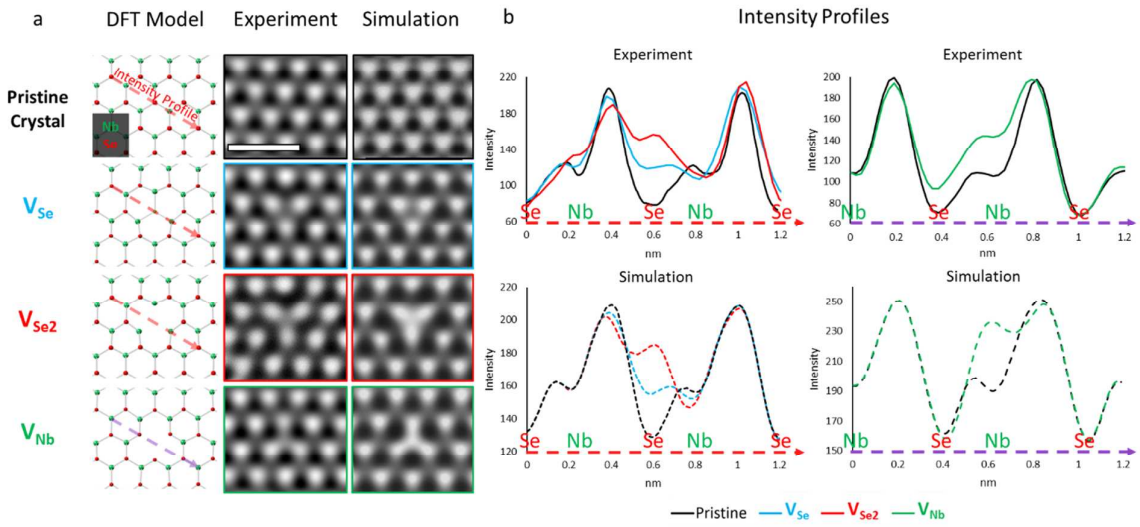

Figure 2: Experimental and simulated images for vacancy point defects in monolayer $NbSe_2$. (a) DFT relaxed structural models (left), high-resolution TEM images (centre) and multislice calculations (right) for pristine material (black border), a Se monovacancy (V_{Se}, blue border), Se divacancy (V_{Se2}, red border) and a Nb vacancy (V_{Nb}, green border) (scale bar: 1nm). (b) Intensity profiles extracted along the armchair direction as shown by arrows in (a) for experiment (upper panels) and simulation (lower panels) demonstrating the ability to distinguish pristine crystal from V_{Se}, V_{Se2} (left) and V_{Nb} vacancies (right) using their individual intensity signatures.

Table 1: Energy change from dissociating a Se divacancy substituted with an impurity X into an impurity substituted monovacancy and a bare monovacancy. The top row V represents a divacancy V_{Se2} dissociating to two monovacancies. Other elements have their usual meanings of hydrogen, carbon, nitrogen, oxygen**.**

Element X	$X_{Se2} \rightarrow (X_{Se}+V_{Se})$
bare (V)	-1.44
H	-0.50
C	0.96
N	1.79
O	1.23

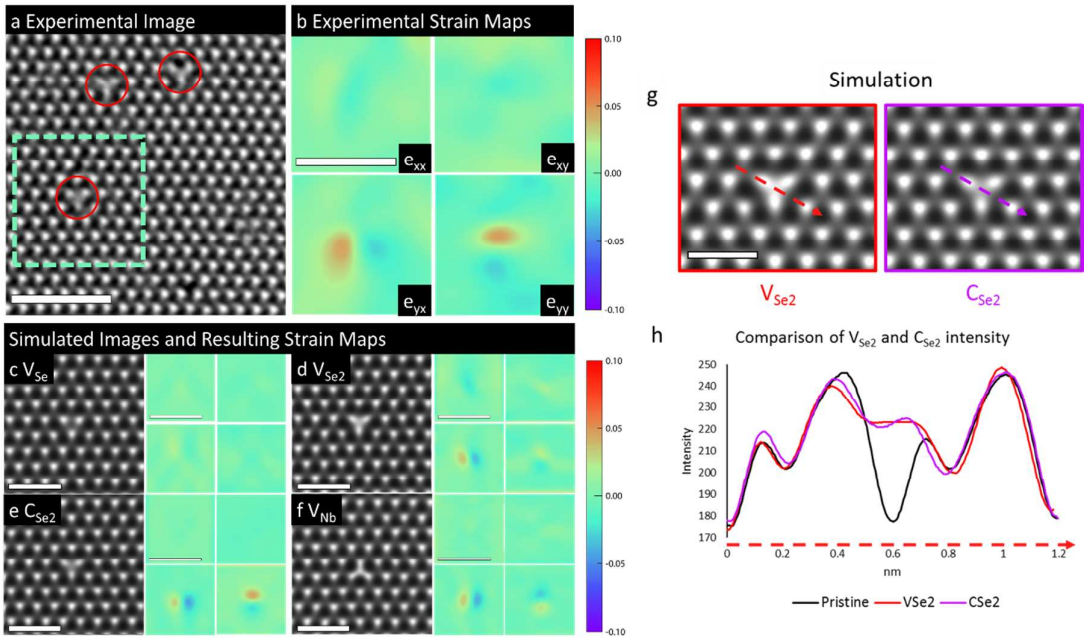

Figure 3: Geometric phase analysis (GPA) allows identification of impurity substitution into Se divacancy defects. (a) TEM image of a region containing three divacancy type defects (circled red) and (b) corresponding strain component maps for representative defect within green box in a). In e_{yx} and e_{yy} regions of tension and compression are observed horizontally and vertically across the defect (scale bars: 2nm). (c-f) GPA strain analysis from TEM image simulations for: (c) a Se monovacancy, V_{Se}; (d) a Se divacancy, V_{Se2}; (e) a carbon substituted Se divacancy, $C_{Se2;}$ and (f) a Nb monovacancy, V_{Nb}. The experimentally observed strain around the defect very closely matches the simulations for a C_{Se2}. (g) TEM image simulations comparing V_{Se2} and C_{Se2}. (h) Intensity profiles from the lines indicated on (g) reveal that TEM image contrast cannot be used to distinguish between these two types of defect. (Scale bars are 1nm for multislice images and 2nm for GPA maps).

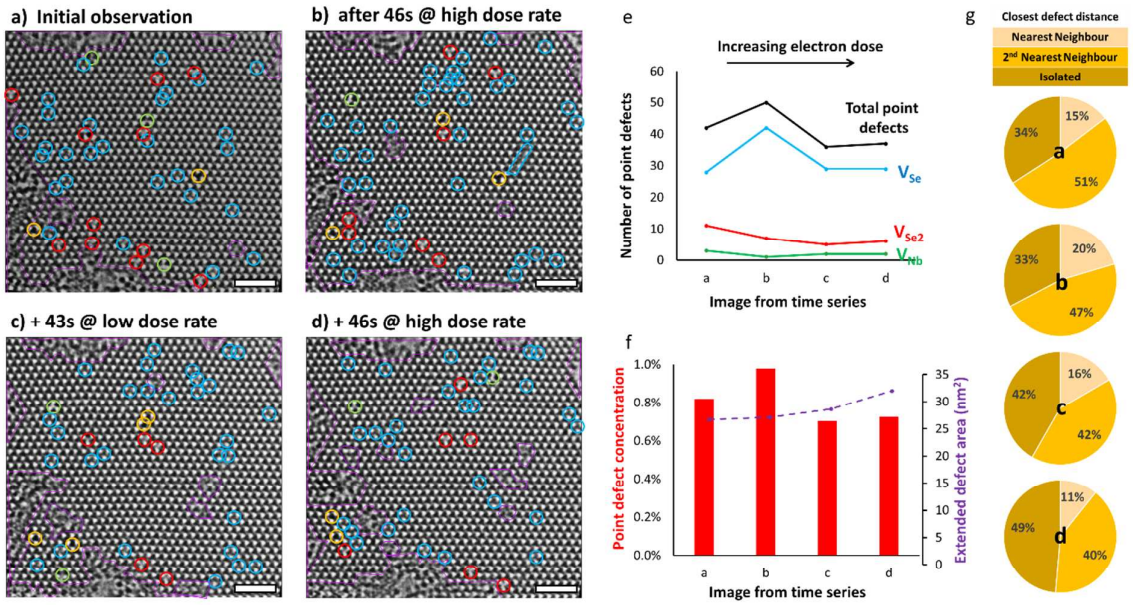

Figure 4: Point defect populations in $NbSe_2$ with continued electron irradiation. Atomic resolution TEM imaging of monolayer $NbSe_2$ (a) on first observation and (b) after continuous imaging with a high dose rate: $1.4x10^6$ e.Å^{-2}s^{-1} for 46s (total dose: $6.5x10^7$e.Å^{-2}). Immediately after acquiring (b) the beam was spread to reduce the electron dose rate to ~$1x10^3$e.Å^{-2} s^{-1}. (c) the same area after 43s of low dose rate imaging (total accumulated dose of $6.5x10^7$e.Å^{-2}) and (d) shows the same area after another 46s of high dose rate imaging (total accumulated dose of $1.3x10^8$e.Å^{-2}). Coloured rings indicate the nature of point defects: Blue: Se monovacancy, V_{Se}; Red: Se divacancy, V_{Se2}; Green: Nb monovacancy, V_{Nb} and Yellow: Pt atom. Purple borders indicate larger, agglomerated regions of defects. Scale bars: 2nm. (e) Summarises the total number of point defects and the total area taken up by larger defect regions in the images (a-d). (f) Plots the percentage of point defects observed in (a-d). (g) Clustering analysis considering the distance between each point defect and its nearest neighbour defect. Any defects separated from their nearest neighbours by more than two nearest neighbour distances are considered to be 'not clustered' (isolated) (See SI Figure S4).

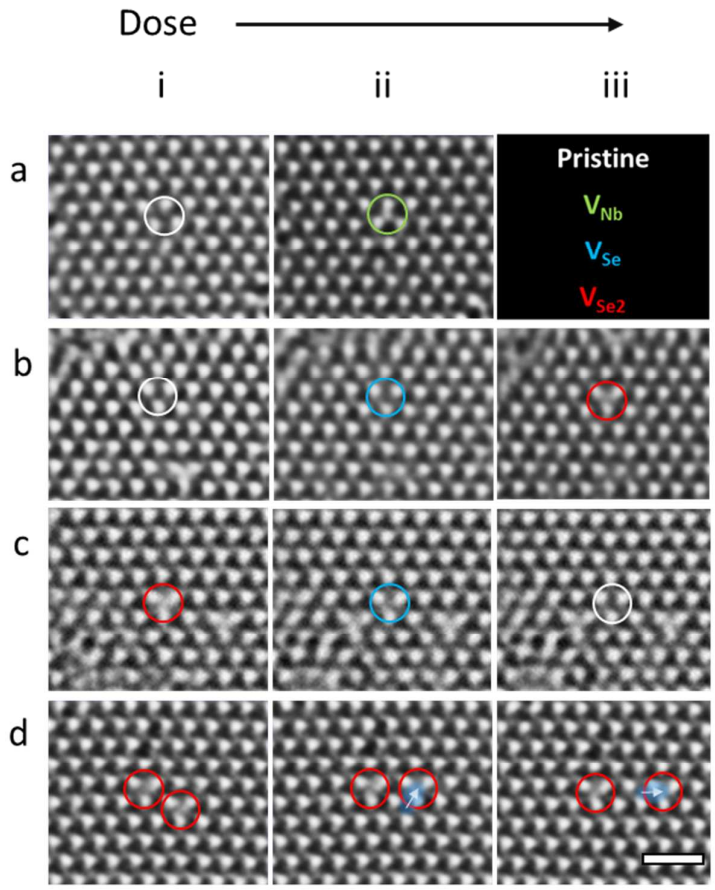

Figure 5: Time series imaging of point defect dynamics in monolayer $NbSe_2$. (a) Formation of an isolated Nb monovacancy (V_{Nb}) in the pristine lattice (at electron doses of $1.3x10^7 e.Å^{-2}$ and $1.6x10^7 e.Å^{-2}$ for (ai) and (aii) respectively). (b) Formation of an isolated V_{Se} monovacancy defect which subsequently transforms to a V_{Se2} divacancy type defect (doses of $3.2x10^6 e.Å^{-2}$, $9.7x10^6 e.Å^{-2}$, and $2.9x10^7 e.Å^{-2}$ for (bi), (bii) and (biii) respectively). (c) A V_{Se2} divacancy type defect which heals to form a V_{Se} monovacancy then to pristine lattice ((at electron doses of $2.0x10^8 e.Å^{-2}$, $2.27\ x10^8 e.Å^{-2}$ and $2.28x10^8 e.Å^{-2}$ for (ci), (cii) and (ciii) respectively). (d) A pair of V_{Se2} divacancies where one hops to adjacent lattice sites. (at electron doses of $1.4x10^8 e.Å^{-2}$, $1.7x10^8 e.Å^{-2}$ and $1.9x10^8 e.Å^{-2}$ for (di), (dii) and (diii) respectively) (scale bar: 1nm).

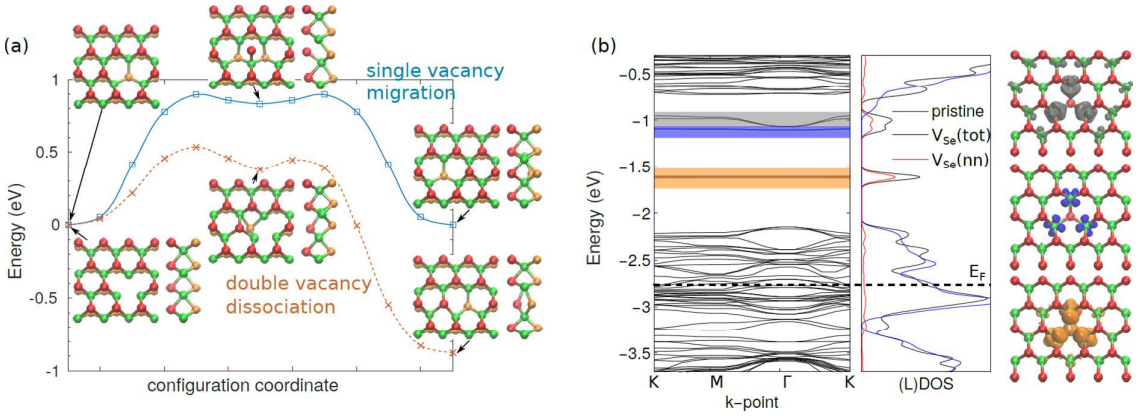

Figure 6: DFT calculations for vacancy migration and their effect on electronic structure. (a) Migration barriers for single vacancy diffusion (squares, blue) and divacancy dissociation to two neighbouring single vacancies (crosses, orange). The lines are guide to the eye. The initial, mid-point, and final atomic structures are also illustrated. (b) Band structure and density of states of the system with V_{Se}. Local DOS from the nearest neighbour Nb atoms to the vacancy and the DOS of pristine $NbSe_2$ are also shown. The localized defect states are visualized on the right as coloured in the band structure.

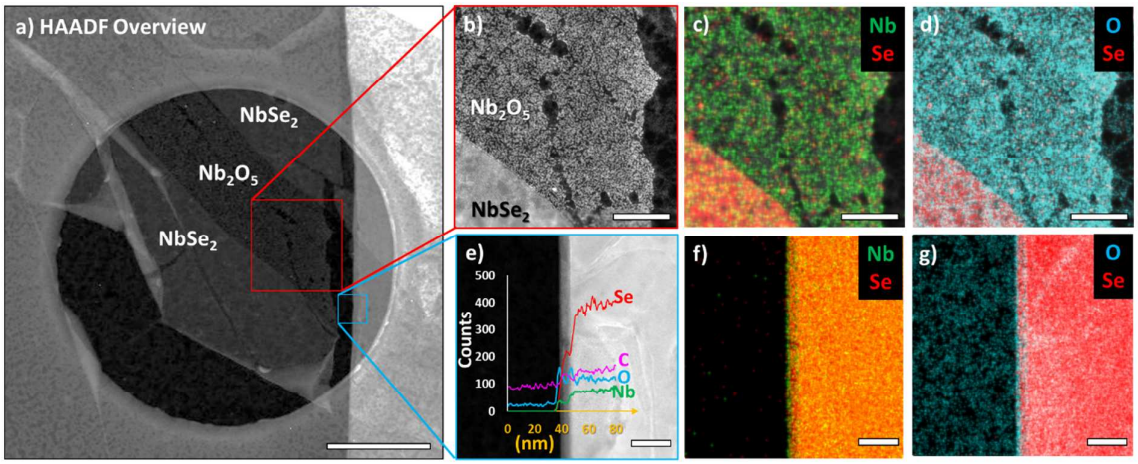

Figure 7: EDX Spectrum imaging revealing regions of oxidation for graphene encapsulated $NbSe_2$ crystals aged for 4 months in ambient conditions. a) HAADF overview of region of interest (scale bar: 500nm) b) HAADF, c) Nb+Se and d) O+Se elemental maps showing that a strip of crystal with a width of ~90 nm is oxidised to form Nb_2O_5 (Scale bar 100nm, see SI for EDX spectrum). e) HAADF, f) Nb+Se and g) O+Se elemental maps showing oxidation of a step flake edge. The enhancement of oxygen is further highlighted by the elemental line profile superimposed on e) (Scale bar: 20nm).

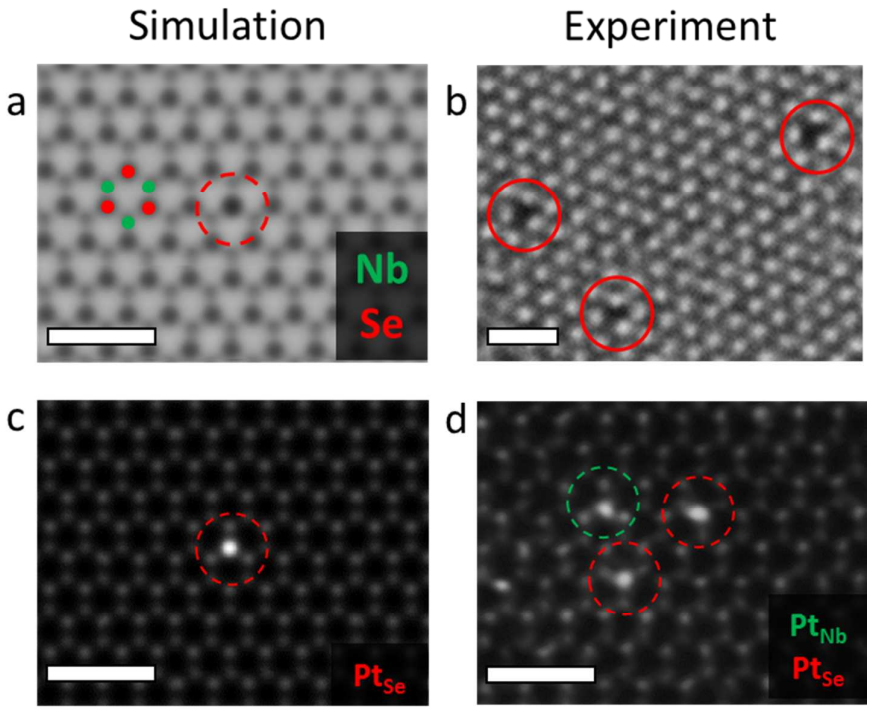

Figure 8: Observation of Pt substitution a) HRTEM image simulation of Pt substitution in a Se site. b) HRTEM experimental image of Pt substitutions into the lattice. c) HAADF STEM simulation of Pt substitution into a Se site, (Pt_{Se}). d) HAADF STEM experimental image of Pt substitutions into both Nb (Pt_{Nb}) and Se (Pt_{Se}) sites. Contrast clearly distinguishes Se columns from Nb and shows the presence of individual Pt atoms associated with both Se and Nb sites in the $NbSe_2$ lattice. All scale bars: 1nm.

Methods/ Experimental:

Encapsulated $NbSe_2$ few layer samples were prepared by mechanical exfoliation in an argon-environment glovebox (levels of H_2O and O_2 below 0.1ppm).[31] Crystals are transferred by a motorised micromanipulation station, which enables micrometre-precision encapsulation within graphene membranes.[31, 41] The exfoliated crystals are typically <10 layers thick and have lateral dimensions up to a few microns. In addition to passivating the crystals, graphene encapsulation also reduces electron beam damage *via* charging or heating effects.[51, 52] To minimise surface contamination, a thin 0.5nm layer of Pt is deposited on the top and bottom of the sample, which can catalytically remove residues when annealed.[60]

Atomic-resolution imaging was performed on an aberration corrected JEOL ARM 200F TEM at 80kV at a constant dose rate of 1.41 x 10^6 $e.A^{-2}s^{-1}$. High-resolution TEM and electron diffraction multi-slice simulations were performed using the JEMS package[68] (accelerating voltage: 80kV; C_c: 1.2mm; C_s: -0.005mm; C_5: 10mm; defocus: 5nm; defocus spread: 5nm and energy spread: 0.81eV). Atomic resolution STEM HAADF imaging of the encapsulated $NbSe_2$ was performed with a FEI Titan 80-200 ChemiSTEM with probe-side aberration correction at 200 kV and X-FEG electron source. STEM experiments were performed with a 21 mrad probe convergence angle and 80 pA probe current. The HAADF detector was collecting electrons scattered between 48 mrad and 191 mrad. HAADF simulations were performed with the QSTEM package.[69] Image processing was performed in Gatan Digital Micrograph software and GPA strain analysis was performed using the in house developed Strain++ program (for further information see SI).

DFT calculations were performed within the projector augmented wave framework, accounting for spin-polarization in the plane-wave basis as implemented in the code VASP.[70, 71] For defect calculations, we used the PBE exchange-correlation functional.[72] 400 eV cutoff for the plane-wave basis yielded converged total energies. Within PBE, the lattice constant for the unreconstructed primitive cell is 3.49 Å. In the case of formation energy calculations, the defects were modeled using the 8x8 supercell and 3x3 k-point mesh. The migration barrier calculations were carried out using a smaller 6x6 supercell and 4x4 k-point mesh.

Author Contributions

The manuscript was written through contributions of all authors. All authors have given approval to the final version of the manuscript. LN and SJH performed diffraction, image simulations, HAADF STEM and EDX experiments, analysed the results and wrote the manuscript. SL helped with the analysis of results. HPK and AK performed DFT calculations and assisted with the discussion of results. EK, RG and IG prepared the samples and assisted with the discussion of the manuscript. RK performed HRTEM imaging of the specimen. JJPP, AMS and JS performed GPA calculations and assisted with discussion of the manuscript.

Supporting Information Available: Additional experimental details including: Electron diffraction and multislice calculation thickness determination, image processing details, DFT of clustering configurations, image simulations of substitutional defects, calculation details on the stability of impurity stabilised Se vacancies, GPA method details, additional GPA defect calculations, displacement cross sections for Se atoms, defect density calculation details, DFT of electronic structure of defects, EDX spectra of Nb_2O_5, diffraction revealing alignment of degraded $NbSe_2$ to crystallographic orientations of graphene, DFT of magnetic properties, DFT of the interaction of graphene encapsulation with $NbSe_2$, LDOS of a Se monovacancy, DFT of atomic CDW and SDW structures and table of defect formation energies.

Supplementary videos 1a-b: HRTEM of the dynamics of point defects.

Supplementary videos 2a-e: HAADF STEM of the dynamic etching of $NbSe_2$ with Pt under the electron beam.

This material is available free of charge *via* the Internet at http://pubs.acs.org.

Acknowledgement: The authors would like to thank the Engineering and Physical Sciences (EPSRC) U.K Grants EP/G035954/1, EP/K016946/1, EP/M010619/1 and EP/J021172/1 and

Defence Threat Reduction Agency Grant HDTRA1-12-1-0013 for funding. Access to aberration corrected electron microscopy was provided through the EPSRC SuperSTEM laboratory (NS/A000016/1). AVK and HPK acknowledge the financial support from the U.S. Army RDECOM *via* contract No. W911NF-15-1-0606 and from the Academy of Finland (Project No. 286279) and through its Centres of Excellence Programme (Project No. 251748). AVK further thanks the Ministry of Education and Science of the Russian Federation for the support in the framework of Increase Competitiveness Program of NUST "MISiS" (#K2-2015-033).

References

1. Geim, A. K. Graphene: Status and Prospects. *Science* 2009, 324, 1530-1534.
2. Novoselov, K. S.; Fal'ko, V. I.; Colombo, L.; Gellert, P. R.; Schwab, M. G.; Kim, K. A Roadmap for Graphene. *Nature* 2012, 490, 192-200.
3. Chhowalla, M.; Shin, H. S.; Eda, G.; Li, L. J.; Loh, K. P.; Zhang, H. The Chemistry of Two-Dimensional Layered Transition Metal Dichalcogenide Nanosheets. *Nat. Chem.* 2013, 5, 263-275.
4. Lehtinen, O.; Komsa, H. P.; Pulkin, A.; Whitwick, M. B.; Chen, M. W.; Lehnert, T.; Mohn, M. J.; Yazyev, O. V.; Kis, A.; Kaiser, U.; Krasheninnikov, A. V. Atomic Scale Microstructure and Properties of Se-Deficient Two-Dimensional MoSe2. *ACS Nano* 2015, 9, 3274-3283.
5. Komsa, H. P.; Kurasch, S.; Lehtinen, O.; Kaiser, U.; Krasheninnikov, A. V. From Point to Extended Defects in Two-Dimensional MoS2: Evolution of Atomic Structure Under Electron Irradiation. *Phys. Rev. B* 2013, 88.
6. Robertson, A. W.; Warner, J. H. Atomic Resolution Imaging of Graphene by Transmission Electron Microscopy. *Nanoscale* 2013, 5, 4079-4093.
7. Lin, Y. C.; Dumcencon, D. O.; Huang, Y. S.; Suenaga, K. Atomic Mechanism of the Semiconducting-to-Metallic Phase Transition in Single-Layered MoS2. *Nat. Nanotechnol.* 2014, 9, 391-396.
8. Komsa, H. P.; Kotakoski, J.; Kurasch, S.; Lehtinen, O.; Kaiser, U.; Krasheninnikov, A. V. Two-Dimensional Transition Metal Dichalcogenides under Electron Irradiation: Defect Production and Doping. *Phys. Rev. Lett.* 2012, 109.
9. Kashtiban, R. J.; Dyson, M. A.; Nair, R. R.; Zan, R.; Wong, S. L.; Ramasse, Q.; Geim, A. K.; Bangert, U.; Sloan, J. Atomically Resolved Imaging of Highly Ordered Alternating Fluorinated Graphene. *Nat. Commun.* 2014, 5, 4902.
10. Lin, Y. C.; Dumcenco, D. O.; Komsa, H. P.; Niimi, Y.; Krasheninnikov, A. V.; Huang, Y. S.; Suenaga, K. Properties of Individual Dopant Atoms in Single-Layer MoS2 : Atomic Structure, Migration, and Enhanced Reactivity. *Adv. Mater.* 2014, 26, 2857-2861.
11. Bangert, U.; Pierce, W.; Kepaptsoglou, D. M.; Ramasse, Q.; Zan, R.; Gass, M. H.; Van den Berg, J. A.; Boothroyd, C. B.; Amani, J.; Hofsass, H. Ion Implantation of Graphene - Toward IC Compatible Technologies. *Nano Lett.* 2013, 13, 4902-4907.
12. Tedstone, A. A.; Lewis, D. J.; O'Brien, P. Synthesis, Properties, and Applications of Transition Metal-Doped Layered Transition Metal Dichalcogenides. *Chem. Mater.* 2016, 28, 1965-1974.
13. Zhao, X.; Chen, P.; Xia, C. X.; Wang, T. X.; Dai, X. Q. Electronic and Magnetic Properties of n-type and p-doped MoS2 Monolayers. *RSC Adv.* 2016, 6, 16772-16778.
14. Wang, H. T.; Wang, Q. X.; Cheng, Y. C.; Li, K.; Yao, Y. B.; Zhang, Q.; Dong, C. Z.; Wang, P.; Schwingenschlogl, U.; Yang, W.; Zhang, X. X. Doping Monolayer Graphene with Single Atom Substitutions. *Nano Lett.* 2012, 12, 141-144.
15. Zhong, L.; Bruno, R. C.; Ethan, K.; Ruitao, L.; Rahul, R.; Humberto, T.; Marcos, A. P.; Mauricio, T. Defect Engineering of Two-Dimensional Transition Metal Dichalcogenides. *2D Mater.* 2016, 3, 022002.
16. Haldar, S.; Vovusha, H.; Yadav, M. K.; Eriksson, O.; Sanyal, B. Systematic Study of Structural, Electronic, and Optical Properties of Atomic-Scale Defects in the Two-Dimensional Transition Metal Dichalcogenides MX2 M = Mo, W; X = S, Se, Te). *Phys. Rev. B* 2015, 92, 235408.
17. González-Herrero, H.; Gómez-Rodríguez, J. M.; Mallet, P.; Moaied, M.; Palacios, J. J.; Salgado, C.; Ugeda, M. M.; Veuillen, J.-Y.; Yndurain, F.; Brihuega, I. Atomic-Scale Control of Graphene Magnetism by Using Hydrogen Atoms. *Science* 2016, 352, 437-441.
18. Han, S. W.; Hwang, Y. H.; Kim, S.-H.; Yun, W. S.; Lee, J. D.; Park, M. G.; Ryu, S.; Park, J. S.; Yoo, D.-H.; Yoon, S.-P.; Hong, S. C.; Kim, K. S.; Park, Y. S. Controlling Ferromagnetic Easy Axis in a Layered MoS2 Single Crystal. *Phys. Rev. Lett.* 2013, 110, 247201.
19. Tongay, S.; Suh, J.; Ataca, C.; Fan, W.; Luce, A.; Kang, J. S.; Liu, J.; Ko, C.; Raghunathanan, R.; Zhou, J.; Ogletree, F.; Li, J.; Grossman, J. C.; Wu, J. Defects Activated Photoluminescence in Two-

Dimensional Semiconductors: Interplay Between Bound, Charged, and Free Excitons. *Sci. Rep.* 2013, 3, 2657.

20. Li, H.; Tsai, C.; Koh, A. L.; Cai, L.; Contryman, A. W.; Fragapane, A. H.; Zhao, J.; Han, H. S.; Manoharan, H. C.; Abild-Pedersen, F.; Norskov, J. K.; Zheng, X. Activating and Optimizing MoS2 Basal Planes for Hydrogen Evolution Through the Formation of Strained Sulphur Vacancies. *Nat. Mater.* 2016, 15, 48-53.

21. El-Bana, M. S.; Wolverson, D.; Russo, S.; Balakrishnan, G.; Paul, D. M.; Bending, S. J. Superconductivity in Two-Dimensional NbSe2 Field Effect Transistors. *Supercond. Sci. Technol.* 2013, 26.

22. Ugeda, M. M.; Bradley, A. J.; Zhang, Y.; Onishi, S.; Chen, Y.; Ruan, W.; Ojeda-Aristizabal, C.; Ryu, H.; Edmonds, M. T.; Tsai, H. Z.; Riss, A.; Mo, S. K.; Lee, D. H.; Zettl, A.; Hussain, Z.; Shen, Z. X.; Crommie, M. F. Characterization of Collective Ground States in Single-Layer NbSe2. *Nat. Phys.* 2016, 12, 92-97.

23. Xi, X. X.; Wang, Z. F.; Zhao, W. W.; Park, J. H.; Law, K. T.; Berger, H.; Forro, L.; Shan, J.; Mak, K. F. Ising Pairing in Superconducting NbSe2 Atomic Layers. *Nat. Phys.* 2016, 12, 139-143.

24. Staley, N. E.; Wu, J.; Eklund, P.; Liu, Y.; Li, L. J.; Xu, Z. Electric Field Effect On Superconductivity in Atomically Thin Flakes of NbSe2. *Phys. Rev. B* 2009, 80.

25. Frindt, R. F. Superconductivity in Ultrathin Nbse2 Layers. *Phys. Rev. Lett.* 1972, 28, 299.

26. Xi, X.; Zhao, L.; Wang, Z.; Berger, H.; Forró, L.; Shan, J.; Mak, K. F. Strongly Enhanced Charge-Density-Wave Order in Monolayer NbSe2. *Nat. Nanotechnol.* 2015, 10, 765-769.

27. Naik, I.; Rastogi, A. K. Charge Density Wave and Superconductivity in 2H-and 4H-NbSe2: A revisit. *Pramana* 2011, 76, 957-963.

28. Huntley, D. J. Charge-Density Waves and Superconductivity in NbSe2. *Phys. Rev. Lett.* 1976, 36, 490-491.

29. Xi, X. X.; Zhao, L.; Wang, Z. F.; Berger, H.; Forro, L.; Shan, J.; Mak, K. F. Strongly Enhanced Charge-Density-Wave Order in Monolayer NbSe2. *Nat. Nanotechnol.* 2015, 10, 765-769.

30. Huang, Y. H.; Chen, R. S.; Zhang, J. R.; Huang, Y. S. Electronic Transport in NbSe2 Two-Dimensional Nanostructures: Semiconducting Characteristics and Photoconductivity. *Nanoscale* 2015, 7, 18964-18970.

31. Cao, Y.; Mishchenko, A.; Yu, G. L.; Khestanova, E.; Rooney, A. P.; Prestat, E.; Kretinin, A. V.; Blake, P.; Shalom, M. B.; Woods, C.; Chapman, J.; Balakrishnan, G.; Grigorieva, I. V.; Novoselov, K. S.; Piot, B. A.; Potemski, M.; Watanabe, K.; Taniguchi, T.; Haigh, S. J.; Geim, A. K.; Gorbachev, R. V. Quality Heterostructures from Two-Dimensional Crystals Unstable in Air by Their Assembly in Inert Atmosphere. *Nano Lett.* 2015, 15, pp 4914–4921.

32. Novoselov, K. S.; Jiang, D.; Schedin, F.; Booth, T. J.; Khotkevich, V. V.; Morozov, S. V.; Geim, A. K. Two-Dimensional Atomic Crystals. *Proc. Natl. Acad. Sci. U.S.A.* 2005, 102, 10451-10453.

33. Two-Dimensional Nanosheets Produced by Liquid Exfoliation of Layered Materials. *Science* 2011, 331, 568.

34. Light-Induced Oxidation of NbSe2 Single Crystals. *J. Phys. Chem. Solids* 1971, 32, 2645.

35. Gao, J.; Li, B.; Tan, J.; Chow, P.; Lu, T.-M.; Koratkar, N. Aging of Transition Metal Dichalcogenide Monolayers. *ACS Nano* 2016, 10, pp 2628–2635.

36. Arguello, C. J.; Chockalingam, S. P.; Rosenthal, E. P.; Zhao, L.; Gutiérrez, C.; Kang, J. H.; Chung, W. C.; Fernandes, R. M.; Jia, S.; Millis, A. J.; Cava, R. J.; Pasupathy, A. N. Visualizing the Charge Density Wave Transition in 2H-NbSe2 in Real Space. *Phys. Rev. B* 2014, 89, 235115.

37. Lovejoy, T. C.; Ramasse, Q. M.; Falke, M.; Kaeppel, A.; Terborg, R.; Zan, R.; Dellby, N.; Krivanek, O. L. Single Atom Identification by Energy Dispersive X-ray Spectroscopy. *Appl. Phys. Lett.* 2012, 100, 154101.

38. D'Alfonso, A. J.; Freitag, B.; Klenov, D.; Allen, L. J. Atomic-Resolution Chemical Mapping Using Energy-Dispersive X-ray Spectroscopy. *Phys. Rev. B* 2010, 81, 100101.

39. Smith, R. J.; King, P. J.; Lotya, M.; Wirtz, C.; Khan, U.; De, S.; O'Neill, A.; Duesberg, G. S.; Grunlan, J. C.; Moriarty, G.; Chen, J.; Wang, J. Z.; Minett, A. I.; Nicolosi, V.; Coleman, J. N. Large-Scale

Exfoliation of Inorganic Layered Compounds in Aqueous Surfactant Solutions. *Adv. Mater.* 2011, 23, 3944-3948.

40. Ibrahem, M. A.; Huang, W. C.; Lan, T. W.; Boopathi, K. M.; Hsiao, Y. C.; Chen, C. H.; Budiawan, W.; Chen, Y. Y.; Chang, C. S.; Li, L. J.; Tsai, C. H.; Chu, C. W. Controlled Mechanical Cleavage of Bulk Niobium Diselenide to Nanoscaled Sheet, Rod, and Particle Structures for Pt-Free Dye-Sensitized Solar Cells. *J. Mater. Chem. A* 2014, 2, 11382-11390.

41. Kretinin, A. V.; Cao, Y.; Tu, J. S.; Yu, G. L.; Jalil, R.; Novoselov, K. S.; Haigh, S. J.; Gholinia, A.; Mishchenko, A.; Lozada, M.; Georgiou, T.; Woods, C. R.; Withers, F.; Blake, P.; Eda, G.; Wirsig, A.; Hucho, C.; Watanabe, K.; Taniguchi, T.; Geim, A. K.; Gorbachev, R. V. Electronic Properties of Graphene Encapsulated with Different Two-Dimensional Atomic Crystals. *Nano Lett.* 2014, 14, 3270-3276.

42. Cowley, J. M.; Moodie, A. F. The Scattering of Electrons by Atoms and Crystals .1. A New Theoretical Approach. *Acta Crystallogr.* 1957, 10, 609-619.

43. Meyer, J. C.; Geim, A. K.; Katsnelson, M. I.; Novoselov, K. S.; Booth, T. J.; Roth, S. The Structure of Suspended Graphene Sheets. *Nature* 2007, 446, 60-63.

44. Hernandez, Y.; Nicolosi, V.; Lotya, M.; Blighe, F. M.; Sun, Z. Y.; De, S.; McGovern, I. T.; Holland, B.; Byrne, M.; Gun'ko, Y. K.; Boland, J. J.; Niraj, P.; Duesberg, G.; Krishnamurthy, S.; Goodhue, R.; Hutchison, J.; Scardaci, V.; Ferrari, A. C.; Coleman, J. N. High-Yield Production of Graphene by Liquid-Phase Exfoliation of Graphite. *Nat. Nanotechnol.* 2008, 3, 563-568.

45. Wu, R. J.; Odlyzko, M. L.; Mkhoyan, K. A. Determining the Thickness of Atomically Thin MoS2 and WS2 in the TEM. *Ultramicroscopy* 2014, 147, 8-20.

46. Castellanos-Gomez, A.; Vicarelli, L.; Prada, E.; Island, J. O.; Narasimha-Acharya, K. L.; Blanter, S. I.; Groenendijk, D. J.; Buscema, M.; Steele, G. A.; Alvarez, J. V.; Zandbergen, H. W.; Palacios, J. J.; Zant, H. S. J. v. d. Isolation and Characterization of Few-Layer Black Phosphorus. *2D Mater.* 2014, 1, 025001.

47. Coleman, J. N.; Lotya, M.; O'Neill, A.; Bergin, S. D.; King, P. J.; Khan, U.; Young, K.; Gaucher, A.; De, S.; Smith, R. J.; Shvets, I. V.; Arora, S. K.; Stanton, G.; Kim, H.-Y.; Lee, K.; Kim, G. T.; Duesberg, G. S.; Hallam, T.; Boland, J. J.; Wang, J. J.; Donegan, J. F.; Grunlan, J. C.; Moriarty, G.; Shmeliov, A.; Nicholls, R. J.; Perkins, J. M.; Grieveson, E. M.; Theuwissen, K.; McComb, D. W.; Nellist, P. D.; Nicolosi, V. Two-Dimensional Nanosheets Produced by Liquid Exfoliation of Layered Materials. *Science* 2011, 331, 568-571.

48. Lin, Y.-C.; Komsa, H.-P.; Yeh, C.-H.; Björkman, T.; Liang, Z.-Y.; Ho, C.-H.; Huang, Y.-S.; Chiu, P.-W.; Krasheninnikov, A. V.; Suenaga, K. Single-Layer ReS2: Two-Dimensional Semiconductor with Tunable In-Plane Anisotropy. *ACS Nano* 2015, 9, 11249-11257.

49. Komsa, H. P.; Krasheninnikov, A. V. Native Defects in Bulk and Monolayer MoS2 from First Principles. *Phys. Rev. B.* 2015, 91, 125304.

50. Haigh, S. J.; Gholinia, A.; Jalil, R.; Romani, S.; Britnell, L.; Elias, D. C.; Novoselov, K. S.; Ponomarenko, L. A.; Geim, A. K.; Gorbachev, R. Cross-Sectional Imaging of Individual Layers and Buried Interfaces of Graphene-Based Heterostructures and Superlattices. *Nat. Mater.* 2012, 11, 764-767.

51. Zan, R.; Ramasse, Q. M.; Jalil, R.; Georgiou, T.; Bangert, U.; Novoselov, K. S. Control of Radiation Damage in MoS2 by Graphene Encapsulation. *ACS Nano* 2013, 7, 10167-10174.

52. Algara-Siller, G.; Kurasch, S.; Sedighi, M.; Lehtinen, O.; Kaiser, U. The Pristine Atomic Structure of MoS2 Monolayer Protected from Electron Radiation Damage by Graphene. *Appl. Phys. Lett.* 2013, 103203107.

53. Hÿtch, M. J.; Snoeck, E.; Kilaas, R. Quantitative Measurement of Displacement and Strain Fields from HREM Micrographs. *Ultramicroscopy* 1998, 74, 131-146.

54. Meyer, J. C.; Eder, F.; Kurasch, S.; Skakalova, V.; Kotakoski, J.; Park, H. J.; Roth, S.; Chuvilin, A.; Eyhusen, S.; Benner, G.; Krasheninnikov, A. V.; Kaiser, U. Accurate Measurement of Electron Beam Induced Displacement Cross Sections for Single-Layer Graphene. *Phys. Rev. Lett.* 2012, 108, 196102.

55. Zan, R.; Bangert, U.; Ramasse, Q.; Novoselov, K. S. Interaction of Metals with Suspended Graphene Observed by Transmission Electron Microscopy. *J. Phys. Chem. Lett.* 2012, 3, 953-958.
56. Berry, V. Impermeability of Graphene and its Applications. *Carbon* 2013, 62, 1-10.
57. Bunch, J. S.; Verbridge, S. S.; Alden, J. S.; van der Zande, A. M.; Parpia, J. M.; Craighead, H. G.; McEuen, P. L. Impermeable Atomic Membranes from Graphene Sheets. *Nano Lett.* 2008, 8, 2458-2462.
58. Hu, S.; Lozada-Hidalgo, M.; Wang, F. C.; Mishchenko, A.; Schedin, F.; Nair, R. R.; Hill, E. W.; Boukhvalov, D. W.; Katsnelson, M. I.; Dryfe, R. A. W.; Grigorieva, I. V.; Wu, H. A.; Geim, A. K. Proton Transport Through One-Atom-Thick Crystals. *Nature* 2014, 516, 227-230.
59. Hanlon, D.; Backes, C.; Doherty, E.; Cucinotta, C. S.; Berner, N. C.; Boland, C.; Lee, K.; Harvey, A.; Lynch, P.; Gholamvand, Z.; Zhang, S.; Wang, K.; Moynihan, G.; Pokle, A.; Ramasse, Q. M.; McEvoy, N.; Blau, W. J.; Wang, J.; Abellan, G.; Hauke, F.; Hirsch, A.; Sanvito, S.; O'Regan, D. D.; Duesberg, G. S.; Nicolosi, V.; Coleman, J. N. Liquid Exfoliation of Solvent-Stabilized Few-Layer Black Phosphorus for Applications Beyond Electronics. *Nat. Commun.* 2015, 6, 8563.
60. Longchamp, J.-N.; Escher, C.; Fink, H.-W. Ultraclean Freestanding Graphene by Platinum-Metal Catalysis. *J. Vac. Sci. Technol., B: Microelectron. Nanometer Struct. Process., Meas., Phenom.* 2013, 31, 020605.
61. Sarkar, D.; Xie, X.; Kang, J.; Zhang, H.; Liu, W.; Navarrete, J.; Moskovits, M.; Banerjee, K. Functionalization of Transition Metal Dichalcogenides with Metallic Nanoparticles: Implications for Doping and Gas-Sensing. *Nano Lett.* 2015, 15, 2852-2862.
62. Giovanni, M.; Poh, H. L.; Ambrosi, A.; Zhao, G.; Sofer, Z.; Sanek, F.; Khezri, B.; Webster, R. D.; Pumera, M. Noble Metal (Pd, Ru, Rh, Pt, Au, Ag) Doped Graphene Hybrids for Electrocatalysis. *Nanoscale* 2012, 4, 5002-5008.
63. Ramasse, Q. M.; Zan, R.; Bangert, U.; Boukhvalov, D. W.; Son, Y.-W.; Novoselov, K. S. Direct Experimental Evidence of Metal-Mediated Etching of Suspended Graphene. *ACS Nano* 2012, 6, 4063-4071.
64. Krivanek, O.; Chisholm, M.; Nicolosi, V.; Pennycook, T.; Corbin, G.; Dellby, N.; Murfitt, M.; Own, C.; Szilagyi, Z.; Oxley, M.; Pantelides, S.; Pennycook, S. Atom-By-Atom Structural and Chemical Analysis by Annular Dark-Field Electron Microscopy. *Nature* 2010, 464, 571-574.
65. Zan, R.; Bangert, U.; Ramasse, Q.; Novoselov, K. S. Metal-Graphene Interaction Studied *via* Atomic Resolution Scanning Transmission Electron Microscopy. *Nano Lett.* 2011, 11, 1087-1092.
66. Hu, X.; Wan, N.; Sun, L.; Krasheninnikov, A. V. Semiconductor to Metal to Half-Metal Transition in Pt-Embedded Zigzag Graphene Nanoribbons. *J. Phys. Chem. C,* 2014, 118, 16133-16139.
67. Rodriguez-Manzo, J. A.; Cretu, O.; Banhart, F. Trapping of Metal Atoms in Vacancies of Carbon Nanotubes and Graphene. *ACS Nano* 2010, 4, 3422-3428.
68. Stadelmann, P. A. EMS - A Software Package for Electron Diffraction Snalysis and HREM Image Simulation In Materials Science. *Ultramicroscopy* 1987, 21, 131-145.
69. Koch, C. T. Determination Of Core Structure Periodicity And Point Defect Density Along Dislocations. PhD, Arizona State University, 2002.
70. Kresse, G.; Joubert, D. From Ultrasoft Pseudopotentials to The Projector Augmented-Wave Method. *Phys. Rev. B.* 1999, 59, 1758.
71. Kresse, G.; Furthmuller, J. Efficiency of Ab-Initio Total Energy Calculations for Metals and Semiconductors Using a Plane-Wave Basis Set. *Comput. Mater. Sci.* 1996, 6, 15.
72. Perdew, J. P.; Burke, K.; Ernzerhof, M. Generalized Gradient Approximation Made Simple. *Phys. Rev. Lett.* 1996, 77, 3865.